Check for updates

Advanced Materials

ADVANCED MATERIALS
www.advmat.de

RESEARCH ARTICLE OPEN ACCESS

Plasmon-Enhanced Second-Harmonic Generation in Atomically Thin Crystalline Silver Nanostructures

Saad Abdullah[1] | Philipp K. Jenke[2] | Andrew P. Weber[1] | Álvaro Rodríguez Echarri[1,3] | Vahagn Mkhitaryan[1] | Fadil Iyikanat[1,4] | Frederik Schiller[5] | Philip Walther[2,6,7] | J. Enrique Ortega[5,8] | Lee A. Rozema[2] | F. Javier García de Abajo[1,9]

[1]ICFO-Institut de Ciencies Fotoniques, The Barcelona Institute of Science and Technology, Castelldefels (Barcelona), Spain | [2]Vienna Center for Quantum Science and Technology (VCQ), Faculty of Physics, University of Vienna, Vienna, Austria | [3]Center for Nanophotonics, NWO Institute AMOLF, XG Amsterdam, The Netherlands | [4]Department of Physics, Dokuz Eylül University, Izmir, Turkey | [5]Centro de Física de Materiales CSIC-UPV/EHU and Materials Physics Center, San Sebastian, Spain | [6]Research Platform for Testing the Quantum and Gravity Interface (TURIS), University of Vienna, Vienna, Austria | [7]Christian Doppler Laboratory for Photonic Quantum Computer, Faculty of Physics, University of Vienna, Vienna, Austria | [8]Departamento de Física Aplicada, Universidad del País Vasco/EHU, San Sebastian, Spain | [9]ICREA-Institució Catalana de Recerca i Estudis Avançats, Barcelona, Spain

Correspondence: Lee A. Rozema (lee.rozema@univie.ac.at) | F. Javier García de Abajo (javier.garciadeabajo@nanophotonics.es)

Received: 26 March 2026 | **Revised:** 11 September 2026 | **Accepted:** 24 September 2026

Keywords: atomically thin metals | crystalline silver nanostructures | nonlinear plasmonics | second-harmonic generation | ultraconfined plasmons

ABSTRACT

The intrinsically weak nonlinear optical response of existing materials, further constrained by symmetry-forbidden second-order processes in centrosymmetric media, severely limits efficient frequency conversion in deeply subwavelength, ultrathin volumes. Addressing this challenge is crucial for the development of nonlinear nanophotonics. Here, we show that atomically thin, epitaxially grown crystalline silver films circumvent these restrictions through the interplay of vertical electronic quantum confinement and lateral plasmonic enhancement. We fabricate atomically thin films that exhibit an enhanced nonlinear response associated with electronic quantum wells, and subsequently pattern them into periodic nanoribbon and nanotriangle arrays sustaining infrared localized surface plasmon resonances. Strong near-field confinement in these structures further boosts second-harmonic generation compared to unpatterned films. Precise control over nanostructure geometry enables spectral tuning of the plasmonic resonance, and consequently, the enhanced harmonic frequency. Our findings establish an approach for activating robust second-order nonlinearities in quantum-confined metals, where intrinsic size effects and plasmonic resonances act synergistically. The compatibility of high-quality epitaxial growth with microchip fabrication technology offers a scalable route toward ultracompact nonlinear optical components for on-chip frequency conversion, sensing, and quantum photonic applications.

1 | Introduction

Since the discovery of nonlinear optical phenomena, considerable effort has been devoted to identifying materials that display substantial nonlinear responses at low optical intensities [1–3]. Traditionally, second-harmonic generation (SHG) has been realized using bulk non-centrosymmetric crystals such as lithium niobate [4, 5], potassium titanyl phosphate [6], or beta-barium borate [7], where symmetry breaking in their crystal structures enables efficient second-order nonlinearities. While these

Saad Abdullah and Philipp K. Jenke contributed equally to this work.

This is an open access article under the terms of the Creative Commons Attribution License, which permits use, distribution and reproduction in any medium, provided the original work is properly cited.
© 2026 The Author(s). *Advanced Materials* published by Wiley-VCH GmbH

materials exhibit comparatively strong nonlinear coefficients, their large interaction volumes and stringent fabrication constraints (including phase-matching requirements) limit their seamless integration with on-chip photonic nanodevices.

To address this challenge, a broad range of alternative SHG platforms has been explored, including plasmonic metamaterials [8–10], two-dimensional (2D) materials [11–13], quantum dots [14, 15], and other emerging nonlinear nanophotonic systems [16–18]. Efforts along these directions have focused on the development of non-centrosymmetric materials and resonant nanophotonic architectures capable of enhancing nonlinear light–matter interactions.

Recent years have witnessed major advances in ultrathin nonlinear optical platforms, including layered ferroelectrics, rhombohedral van der Waals crystals, dielectric metasurfaces, and hybrid resonant nanostructures. For example, ferroelectric $NbOI_2$ nanosheets have demonstrated effective nonlinear susceptibilities approaching the 10^3 pm/V range together with peak-intensity-normalized SHG conversion efficiencies exceeding 0.2% under resonant excitation conditions [19], while rhombohedral 3R-MoS_2 structures have exhibited resonantly enhanced nonlinear susceptibilities approaching ~ 800 pm/V together with SHG enhancement factors exceeding two orders of magnitude in resonant nanodisk geometries [20]. More recently, periodically poled layered semiconductor structures based on 3R-MoS_2 have enabled quasi-phase-matched nonlinear frequency conversion efficiencies approaching the 0.1% range over micrometre-scale interaction lengths [13]. Likewise, dielectric metasurfaces and quasi-bound-state-in-the-continuum architectures integrated with layered semiconductors have demonstrated SHG enhancement factors exceeding 10^3 through strong resonant field confinement [21].

While each of these novel nonlinear platforms offers distinct advantages and enhancement mechanisms, atomically thin crystalline noble metals provide access to a complementary nonlinear nanophotonic regime in which conduction electrons are vertically confined, giving rise to quantum finite-size effects and the formation of quantum-well states (QWS) that modify the metallic electronic band structure and can enhance the nonlinear optical response [22–27]. In parallel, plasmonic resonances supported by such ultrathin crystalline metallic films sustain high-quality, deep-subwavelength optical confinement at visible and near-infrared frequencies [28, 29]. Combined with additional lateral field enhancement enabled through nanopatterning, these ultrathin crystalline metallic nanostructures support enhanced SHG together with strong optical near-field confinement, tunable plasmonic resonances, scalable fabrication, and direct compatibility with silicon-based nanophotonic architectures.

The geometry and size of nanostructures critically influence their plasmonic behavior [30]. Precise control over these parameters is essential to ensure that localized plasmon resonances match the excitation conditions required for efficient nonlinear conversion. A variety of techniques have been developed to meet such fabrication demands, including ion-beam milling [31], colloidal synthesis [32], self-assembly organization [33], electrochemical deposition [34], and vapor deposition methods [35], among others. While each approach offers distinct advantages, they often fall short in resolution, spatial control, or substrate compatibility when applied to subnanometer-scale volumes. In addition, achieving high-quality, scalable, and tunable plasmonic resonances that enhance the local field strength also requires minimizing losses, particularly in metallic films, which often require tuning the deposition parameters [36].

In this work, we overcome fabrication challenges by combining epitaxially grown ultrathin silver films with precise lateral patterning of periodic nanostructures [28, 29] to achieve an efficient nonlinear optical response. Using high-resolution electron-beam lithography (EBL), we fabricate well-defined planar arrays of crystalline silver nanostructures that enable tunable plasmonic resonances featuring high quality factors and deep-subwavelength confinement. Large boosts in SHG are observed, driven by vertical electronic confinement and lateral plasmonic enhancement associated with their atomic-scale thickness (Figure 1). Specifically, we fabricate crystalline silver ribbons and triangles with thicknesses ranging from 7 to 14 monolayers (MLs) (i.e., $\sim 1.7 - 3.3$ nm thickness), (111) surface orientation, widths in the $W = 50 - 400$ nm range, and periods $P = 3W$. The epitaxial growth of the metal film, followed by surface passivation with $3 - 4$ MLs of gold, bears critical importance to minimize the density of defects and grain boundaries, resulting in high plasmon quality, low optical damping, and enhanced SHG. Our results establish a promising strategy for integrating strong nonlinearities into nanophotonic architectures, advancing the long-standing goal of realizing efficient nonlinear optical devices.

2 | Results

We focus on the nonlinear optical properties of atomically thin (few-monolayer) epitaxially grown crystalline silver films of (111) surface orientation capped with a few monolayers of gold (see Methods). The gold capping layer, which closely matches the lattice constant of silver, grows epitaxially and enhances the structural stability of the heterostructure while preventing oxidation of the underlying silver. The growth protocol is optimized to produce high-quality crystalline films, as explained elsewhere [28]. Achieving ultrathin noble-metal layers that are simultaneously stable and possess high crystalline quality is generally not feasible with conventional thin-film deposition techniques such as sputtering [37] or wet-chemical synthesis [38], although recent approaches based on atomic-level precision chemical etching have demonstrated nanometer-scale control [26].

Here, we employ epitaxy, which provides a robust and reproducible route to synthesize atomically smooth and laterally uniform films, which are crucial for sustaining coherent plasmonic and nonlinear optical responses in a platform suitable for nanophotonic applications. As an indication of the film quality, we clearly observe nearly parabolic electronic bands in angle-resolved photoemission spectroscopy (Figures 1b and S1), associated with vertical QWS in the metallic films [39]. The separation between QWS allows us to determine the number of (111) atomic layers in each film, narrowly distributed around a central value; otherwise, in a much thicker (bulk-like) film, the discrete sub-bands overlap due to inhomogeneous broadening, effectively approaching a continuum-like response. The epitaxial growth mechanism, implemented under carefully controlled

15214095, 0, Downloaded from https://advanced.onlinelibrary.wiley.com/doi/10.1002/adma.75217 by Centrum Voor Wiskunde En Info (Cwi), Wiley Online Library on [11/11/2026]. See the Terms and Conditions (https://onlinelibrary.wiley.com/terms-and-conditions) on Wiley Online Library for rules of use; OA articles are governed by the applicable Creative Commons License

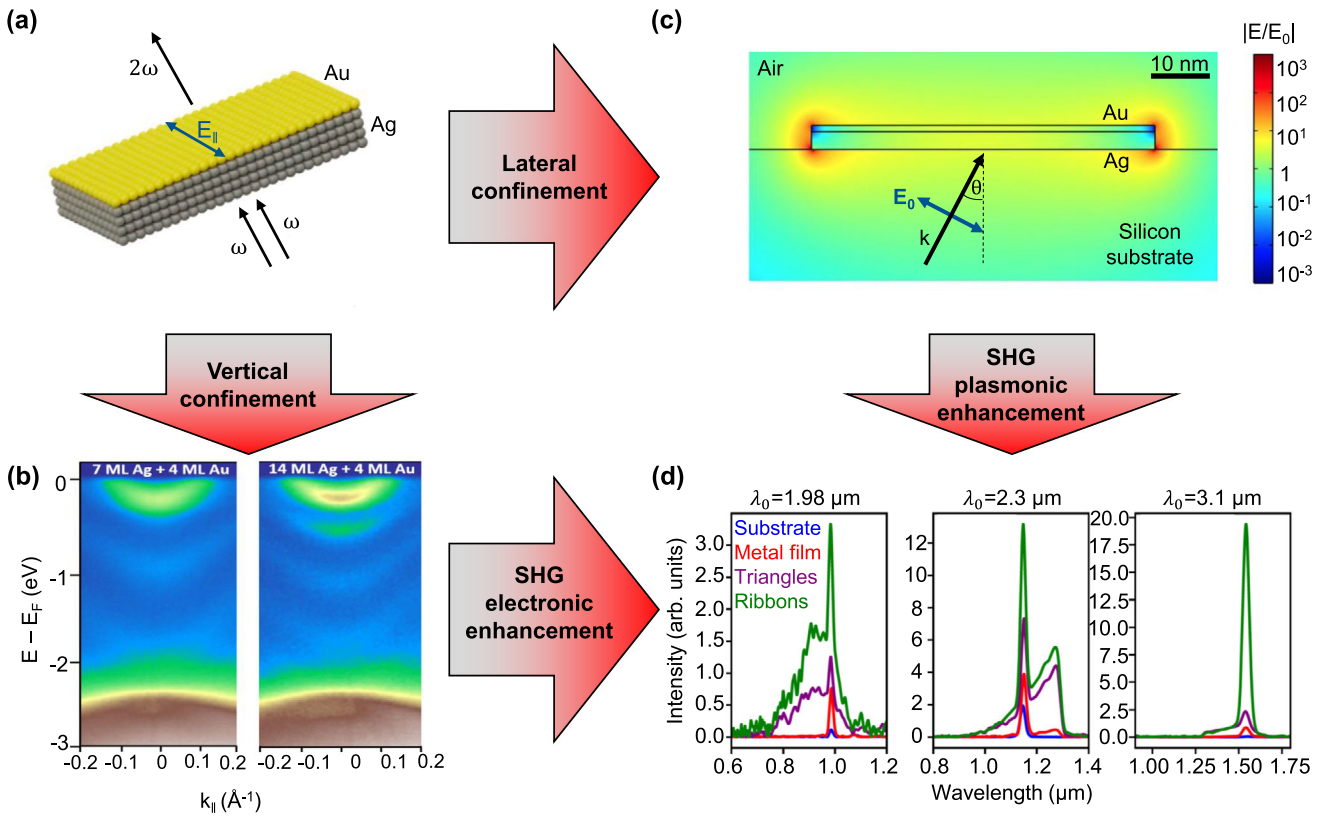


FIGURE 1 | Plasmon-enhanced second-harmonic generation (SHG) in ultrathin crystalline silver films. General scheme illustrating the generation of an enhanced second-harmonic signal driven by vertical electronic confinement and lateral plasmonic near-field enhancement. (a) We consider atomically thin crystalline metal nanoribbons capped with gold. Pairs of incident photons at the fundamental frequency ω are converted into second-harmonic photons at frequency 2ω. The input and output light polarizations are oriented across the ribbons. (b) Dispersion diagrams of electronic quantum wells in the metal revealed through angle-resolved photoemission spectroscopy (ARPES) performed on films consisting of 7 and 14 Ag(111) monolayers (MLs), capped with 4 MLs of Au(111) each. (c) Electric near-field enhancement in response to plane-wave illumination calculated for p-polarized light incident with an angle $\theta \approx 13°$ and field amplitude $\mathbf{E}_0$. (d) Measured SHG intensity spectra at different excitation wavelengths λ_0 (see labels) for various nanostructure geometries, including the bare silicon substrate and the unstructured metal film for reference, as well as periodic ribbon and triangle arrays. The metal thickness is 7+4 MLs of Ag+Au. The ribbon width and triangle side are $W = 150$ nm for $\lambda_0 = 3.1\mu$m and $W = 110$ nm for the two other wavelengths, while the period is $3\,W$ in both cases.

pressure and temperature conditions, enables the deposition of high-quality, low-loss crystalline metal films (see Methods). We visualize the presence and density of QWS in Figure 1b by comparing angle-resolved photoemission spectroscopy (ARPES) measurements of ultrathin films with two different thicknesses (7 and 14 MLs of silver). We aim to exploit the vertical confinement of conduction electrons in these films to enhance SHG [27]: as the film becomes thinner, electronic states are increasingly quantized in the out-of-plane direction, giving rise to more widely separated QWS (Figure 1b); this enhanced level spacing produces a more atomic-like optical response and, consequently, stronger nonlinear behavior; in this regime, the out-of-plane electron dynamics departs from the quasi-harmonic behavior characteristic of the bulk metal; equivalently, the QWS no longer resemble the nearly equally spaced ladder states of a parabolic potential.

It is also well established that nonlinearities can be boosted in nanoparticles through the mediation of plasmonic resonances [40–42], which strongly enhance the near field, creating favorable conditions for efficient SHG. To harness this effect, we pattern our epitaxially grown crystalline metal films into periodic nanostructures using EBL, enabling precise control over the lateral geometry (i.e., shape, size, and periodicity; see Figure S2) and the resulting plasmonic resonances. At the plasmon frequency, the electric near field can be substantially enhanced relative to the incident field, as schematically illustrated for a dipolar resonant ribbon in Figure 1c.

In this work, we combine these two approaches (i.e., vertical electronic confinement provided by atomically thin crystalline metal films and lateral plasmonic confinement introduced through electron-beam patterning of the same films) to produce a strong second-harmonic response from otherwise centrosymmetric noble-metal crystals. As illustrated schematically in Figure 1d, we investigate SHG under different excitation wavelengths from silver ribbons with thicknesses of only a few atomic monolayers (7 ML silver capped with 4 ML of gold in this figure) and lateral widths ranging from tens to hundreds of nanometers. The response of nanoribbon arrays is compared with that of extended films, the substrate signal, and nanotriangles of similar lateral dimensions. The presence of an unpatterned metal film produces a large boost in the SHG signal relative to the bare substrate, while

15214095, 0, Downloaded from https://advanced.onlinelibrary.wiley.com/doi/10.1002/adma.75217 by Centrum Voor Wiskunde En Info (Cwi), Wiley Online Library on [11/11/2026]. See the Terms and Conditions (https://onlinelibrary.wiley.com/terms-and-conditions) on Wiley Online Library for rules of use; OA articles are governed by the applicable Creative Commons License

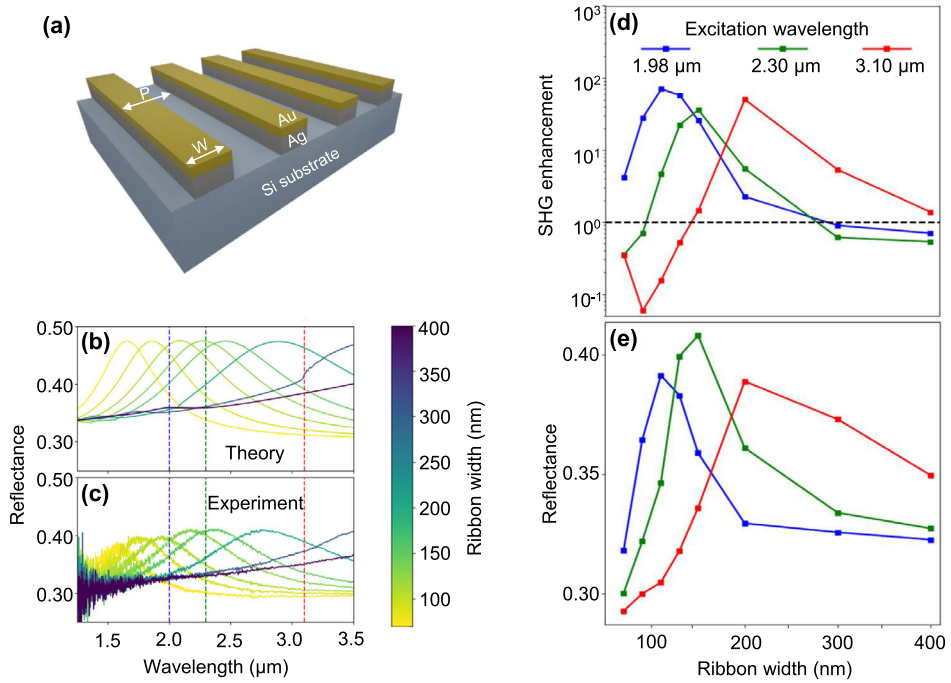


FIGURE 2 | Spectral and geometrical dependence of SHG enhancement. (a) Scheme of the structures under consideration, consisting of Au-capped Ag-ribbon arrays (width W, period $P = 3\,W$). (b,c) Calculated and FTIR-measured reflectance spectra for different ribbon widths. (d) Measured SHG enhancement of the ribbon arrays relative to the SHG signal of the homogeneous metal film for three different incident light wavelengths λ_0 as a function of ribbon width. (e) FTIR-measured reflectance at the three excitation wavelengths for the same sample as in (d). Silver ribbons lie on a Si substrate, have a fixed thickness of 11 MLs of Ag(111), and are capped with 4 MLs of Au(111).

lateral nanostructuring further enhances the nonlinear response, with the highest enhancement found for ribbons. The effect is strongly wavelength-dependent, as illustrated by the presence of additional spectral structure adjacent to the second-harmonic wavelength when the fundamental wavelength is $\lambda_0 = 1.975$ or $2.3\,\mu$m, in contrast to the sharper response for $\lambda_0 = 3.1\,\mu$m. In the following, we present a more quantitative study of the SHG generated by atomically thin silver nanoribbons, considering only the SHG signal originating from the region of interest and neglecting any residual contributions observed in the spectra shown in Figure 1d.

To investigate the enhancement of SHG through engineered plasmonic resonances, we fabricated a set of periodic silver ribbon arrays on a silicon substrate. The period-to-width ratio was set to $P/W = 3$ (see Figure 2a). In the fabrication process, the width W was varied from 50 to 150 nm in steps of 20 nm, and from 150 to 400 nm in steps of 50 nm. We also examined the thickness dependence of SHG by comparing silver films of 7, 11, and 14 ML ($\sim$1.65, $\sim$2.60, and $\sim$3.31 nm, respectively), each of them capped with 4 ML of Au ($\sim$1 nm). Representative secondary-electron-emission (SEM) images are shown in Figure S2.

To determine the spectral position of the plasmonic resonances, we first simulated the reflectance spectra (see Methods) and then validated the results experimentally using Fourier-transform infrared spectroscopy. Measurements were performed over a broad infrared spectral range from 1.2 to 5 μm, using a gold mirror as a reference. Simulated and measured reflectance spectra are plotted in Figure 2b, c, respectively, for ribbons patterned on 11 ML silver films with increasing widths (colored curves), showing a good overall agreement. The small discrepancies in peak amplitude likely arise from experimental imperfections, including defects in the silver layer, small deviations from the nominal ribbon dimensions, and limitations associated with the EBL fabrication process. We corroborate a scaling of the light wavelength at which the plasmon emerges as $\propto \sqrt{W/d}$ with ribbon width W and film thickness d, as predicted in a previous study [28]. Such a scaling is maintained for all film thicknesses under consideration (see Figure S3). Based on these results, we correlate the linear optical response with the nonlinear optical measurements, as discussed below.

The resonant plasmonic ribbons significantly enhance the SHG efficiency compared with a planar metal film of the same thickness (see Figure 2d). Note that this enhancement originates from the response of the ribbons to polarization along their width, as confirmed by examining the dependence of the SHG signal on the polarization of both the exciting light and the generated output (see Figure S4). In particular, we focus our nonlinear measurements on excitation wavelengths of 1.98, 2.3, and 3.1 μm. The largest enhancements for each excitation wavelength occur when the ribbon width is resonant with the fundamental (excitation) wavelength (cf. Figure 2d, e). These results corroborate that near-field enhancement in plasmon-resonant structures increases the SHG signal. Conversely, for ribbon widths that are off-resonance at a given excitation wavelength, the SHG response can be even weaker than that of a planar metal film of the same thickness. We attribute this reduction to the smaller effective lateral interaction area of the ribbons compared with a continuous planar film when

15214095, 0, Downloaded from https://advanced.onlinelibrary.wiley.com/doi/10.1002/adma.75217 by Centrum Voor Wiskunde En Info (Cwi), Wiley Online Library on [11/11/2026]. See the Terms and Conditions (https://onlinelibrary.wiley.com/terms-and-conditions) on Wiley Online Library for rules of use; OA articles are governed by the applicable Creative Commons License

no plasmonic enhancement is present. Absolute SHG powers are shown in Figure S5 for 2.3 μm excitation as a function of the average pump power. A clear quadratic dependence is observed in the intermediate regime, followed by saturation at sufficiently high powers. Using an analysis analogous to that reported in Ref. [27] for unpatterned films, these results correspond to large effective SHG susceptibilities.

We further compare the experimentally measured and theoretically calculated enhancement ratio of the SHG signals produced by ribbon-patterned and unpatterned films for Ag films of three different thicknesses (7, 11, and 14 ML silver, from top to bottom, respectively, all coated with 4 ML gold) as a function of the ribbon width W and for excitation wavelengths $\lambda_0 = 1.98\,\mu m$ (left), 2.3 μm (center), and 3.1 μm (right).

For the experimental data (solid curves), the enhancement factor is obtained by normalizing the peak SHG power measured from the patterned ribbon arrays to that measured from an unpatterned film of the same thickness under identical illumination conditions. The SHG conversion efficiencies of the unpatterned silver films, which serve as the reference for the reported enhancement factors, are shown in Figure S8. The procedure used to extract the SHG conversion efficiencies is illustrated in Figure S5, following the model described in Ref. [27].

In the theoretical calculations, owing to the centrosymmetric crystallographic structure of the bulk metal, we describe the SHG signal in terms of the nonlinear surface susceptibility, which is assumed to be local, independent of crystallographic orientation, dominated by the normal component $\chi^{SHG}_{\perp\perp\perp}$, and unaffected by film nanostructuring. Under these assumptions, the susceptibility enters as an overall multiplicative factor in the calculation of the far-field SHG amplitude and, consequently, cancels when taking the ratio of the nonlinear intensities generated by patterned and unpatterned films. The induced second-harmonic surface polarization density is given by the product of the nonlinear susceptibility and the square of the normal component of the fundamental near field, and is therefore also directed normal to the surface. By virtue of reciprocity, the far-field amplitude generated by this polarization density at the detector position can be evaluated from the surface-normal field induced by a plane wave incident from the detector direction at the second-harmonic frequency. The nonlinear signal is thus obtained from the surface integral of the squared fundamental surface-normal near field multiplied by the reciprocity-related second-harmonic surface-normal near field (see Methods). Given the in-plane translational invariance of the samples under the illumination conditions considered here, this surface integral reduces to a contour integral (see Figure S10).

The dependence of the SHG enhancement on ribbon width is in qualitative agreement with theory for all excitation wavelengths and film thicknesses considered. The enhancement is peaked at wavelength- and thickness-dependent ribbon widths that are also consistent with the resonances identified from the reflectance of the structured films (Figure 3j–l). The SHG enhancement exhibits a significantly more pronounced modulation than the FTIR reflectance, as expected from the nonlinear nature of the process. In addition, the finite spectral bandwidth associated with the pulsed excitation can be neglected relative to the spectral width of the underlying plasmonic resonances. Some discrepancies in magnitude are observed between the experimental and theoretical enhancement ratios. These discrepancies are generally smaller than one order of magnitude, except for the thinnest film thickness at the shortest wavelength. We attribute them primarily to simplifications in the theoretical model, which ignores nonlocal effects and assumes a uniform nonlinear susceptibility that is independent of crystallographic orientation and unaffected by the strong surface-curvature variations at the ribbon edges. Additional effects not included in the model may also contribute, including quantum finite-size effects that modify the surface response, particularly at the smallest thicknesses, as well as imperfections in the fabrication process.

Overall, the observed SHG behavior is consistent with that expected from localized plasmon resonances, as the highest enhancements are observed where the linear reflectance is peaked (Figure 3j–l), corresponding to ribbons that are resonant at the respective values of the incident wavelength λ_0, undergoing plasmon-enhanced local-field confinement. As the ribbon width deviates from the resonance condition, the SHG signal gradually decreases due to the reduced overlap between the fundamental mode and the plasmonic resonance. This behavior highlights the critical role of geometrical tuning in achieving optimal nonlinear conversion. By systematically engineering the ribbon width, SHG can be selectively enhanced at specific excitation wavelengths, providing a versatile degree of tunability in plasmon-enhanced nonlinear structures. The present results should stimulate quantitative predictions of the SHG yield from full electronic-structure calculations that account for the surrounding environment and track the many-body dynamics of thin crystalline metallic structures under strong external illumination.

The SHG enhancement discussed in Figure 3 focuses on nanoribbon arrays. Comparable and consistent behavior is observed for other geometries, such as periodic nanotriangles (Figure S6), with similar trends after normalization by the metal filling fraction, reflecting geometry-dependent field confinement.

3 | Conclusions

In summary, we have demonstrated a double mechanism for SHG enhancement from laterally patterned ultrathin crystalline metallic films: on top of the nonlinear enhancement associated with vertical quantum confinement of conduction electrons [27], we observe plasmonic confinement associated with plasmon resonances that produce strong lateral optical-field confinement in patterned nanostructures. We based our results on experimental measurements in good agreement with electromagnetic simulations. Similar levels of SHG enhancement are observed for different types of structures, such as ribbon and triangle arrays, which are compared in Figure S6. A key ingredient in this study has been the stability of the films, consisting of 7-14 ML of silver passivated with 4 ML of gold. Looking ahead, lateral engineering of the patterned nanostructures could produce even larger enhancement, including double resonances (i.e., at both the fundamental and the second-harmonic frequencies). Lattice resonances in periodic structures could produce additional boosts of the SHG signal. Other frequency-conversion processes, including spontaneous parametric down-conversion,

15214095, 0, Downloaded from https://advanced.onlinelibrary.wiley.com/doi/10.1002/adma.75217 by Centrum Voor Wiskunde En Info (Cwi), Wiley Online Library on [11/11/2026]. See the Terms and Conditions (https://onlinelibrary.wiley.com/terms-and-conditions) on Wiley Online Library for rules of use; OA articles are governed by the applicable Creative Commons License

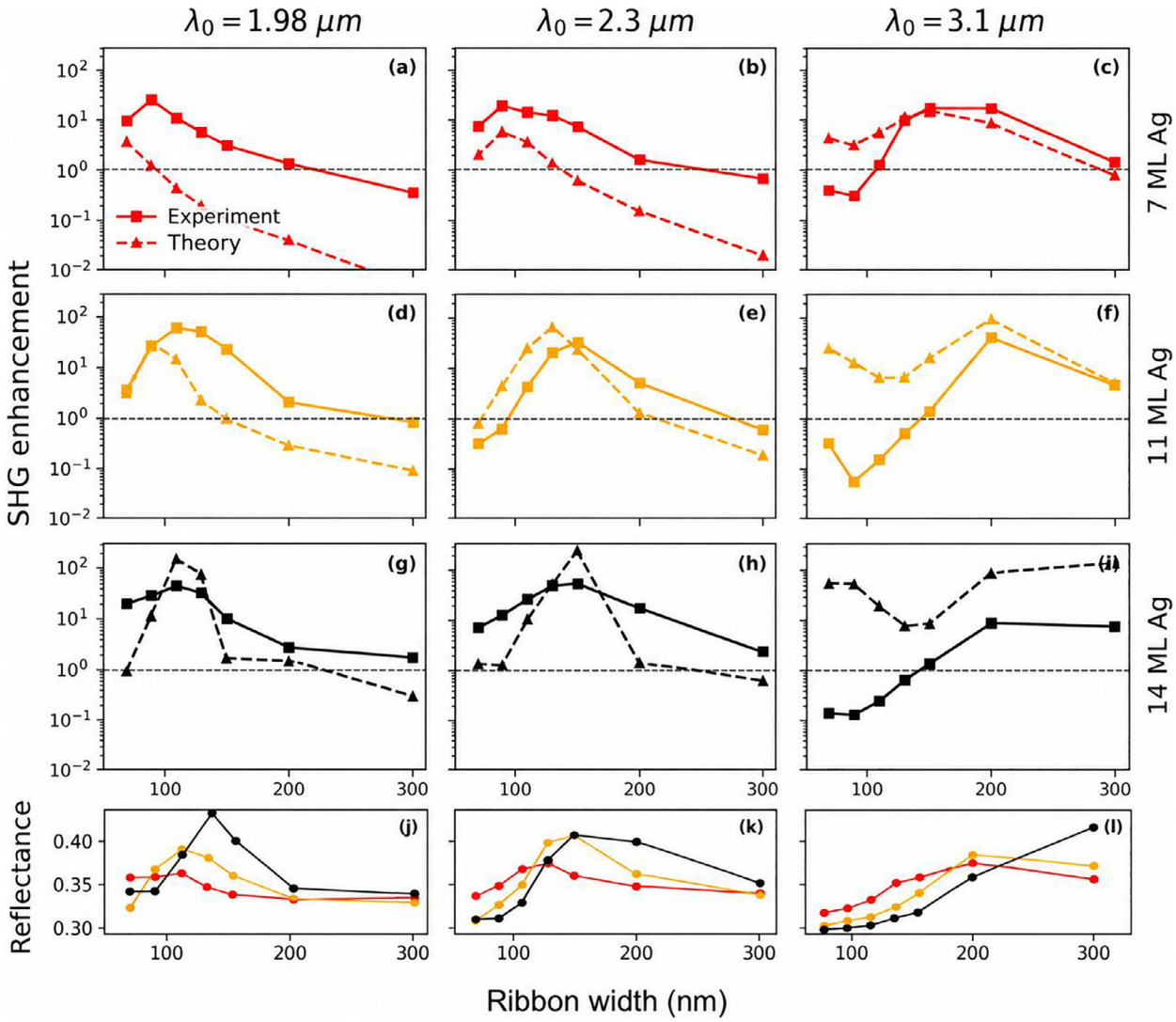


FIGURE 3 | Variation of SHG enhancement with Ag film thicknesses. (a–i) Experimentally measured (solid curves) and theoretically estimated (dashed curves) SHG enhancement, referenced to the corresponding unpatterned ultrathin metal film, as a function of ribbon width for different film thicknesses (7 ML (a–c), 11 ML (d–f), and 14 ML (g–i) of Ag) and incident light wavelengths (λ_0 = 1.98 μm (a,d,g), 2.3 μm (b,e,h), and 3.1 μm (c,f,i)). All samples are coated with 4 ML Au. (j–l) Measured reflectance at the SHG excitation wavelengths as a function of ribbon width for the thicknesses considered in panels (a–i) (color-coordinated curves) at the same fundamental excitation wavelengths.

should also be explored to take advantage of the strong spatial confinement offered by patterned ultrathin metallic films, with potential applications in nanoscale lasers and field amplifiers. Overall, these results offer a promising route toward integration of ultrathin nonlinear plasmonic platforms into sophisticated silicon photonic circuits, enabling on-chip frequency doubling and other nonlinear optical functionalities. Such systems are amenable to miniaturization and tuning, rendering them strong candidates for next-generation nanophotonic devices.

4 | Methods

4.1 | Fabrication of Atomically Thin Silver Films

Crystalline gold-capped silver films were deposited in an ultra-high vacuum (UHV) chamber with a base pressure of 1.0×10^{-10} mbar on substrates consisting of $4 \times 12\,mm^2$ n-doped Si(111) chips with a resistivity of 120 – 340 Ωcm, corresponding to a dopant concentration of $1.3 - 3.7 \times 10^{13} cm^{-3}$. This doping concentration ensured a sufficient electrical conductivity for surface science applications and smooth deposition without compromising the plasmonic and optical performance of the Ag–Au hybrid films.

For the processing of the films, the Si(111) substrates were first degassed overnight in UHV at 900K, and then flashed to 1400K for 20 – 30 s to remove the native oxide layer. The temperature was subsequently lowered to 600 K, maintained for 30 min, and then cooled to room temperature, producing an atomically clean, defect-free Si(111) surface with a 7×7 reconstruction.

Silver atoms were evaporated from an electron-bombardment evaporator, with the deposition rate calibrated to sub-monolayer accuracy using a quartz crystal microbalance, and verified by photoemission probing of the characteristic 1 – 2 ML Ag(111)

15214095, 0, Downloaded from https://advanced.onlinelibrary.wiley.com/doi/10.1002/adma.75217 by Centrum Voor Wiskunde En Info (Cwi), Wiley Online Library on [11/11/2026]. See the Terms and Conditions (https://onlinelibrary.wiley.com/terms-and-conditions) on Wiley Online Library for rules of use; OA articles are governed by the applicable Creative Commons License

surface states [43]. Film growth followed a two-step procedure: Ag was deposited with the substrate cooled to 100 − 120 K, and then slowly annealed to room temperature [44]. The typical deposition rate was ∼ 0.3 ML/min, although comparable quality was obtained for rates between 0.1 and 0.5 ML/min. A few (∼ 4) MLs of gold were then deposited for film passivation. The deposition temperature, maintained near 100 K, was found to be the key parameter for achieving high-quality films. Scanning tunneling microscopy was also used to verify that the surface exhibits sub-atomic-monolayer RMS roughness (Figure S9).

4.2 | Fabrication of Periodic Nanostructure Arrays

Periodic nanoribbons and nanotriangles of varying sizes were fabricated from these crystalline Ag–Au thin films using a CRESTEC EBL system. The films were first spin-coated with a negative-tone ARN 7520.07 resist at an angular velocity of 4000 revolutions per minute for 1 min, yielding a final resist thickness of ≈ 150 nm. To preserve metal film quality, no baking was applied after spin-coating. The electron-beam source was operated at 50 keV with a current of 50 pA. The area dose of the ARN 7520.07 resist was set to 400 $\mu C/cm^2$. An optimum dwell time of 0.7 μs was found from a series of test exposures covering the 0.1 − 1.0μs range around the theoretical estimate of 0.72 μs. These tests were carried out by fixing the write field of the EBL exposure at 60 μm with a discretization step of 6 nm. Patterns were exposed in a raster-scanning mode. EBL-exposed regions in the chips were developed by immersion in an AR 300-73 developer for 1.5 min, followed by immersion in DI water for 30 s. The exposed regions resulted in the formation of a patterned resist mask according to the geometrical requirements of the particular nanoparticle arrays. Pattern transfer was carried out by argon plasma dry etching in an Oxford PlasmaLab 80 Plus reactive ion etching (RIE) system, where physical sputtering removed the unprotected Ag–Au thin film regions, thereby yielding the final nanoparticle arrays.

4.3 | Optical Characterization

Plasmon spectra were acquired in the far field using a Bruker Hyperion Fourier-transform infrared (FTIR) spectrometer operating over a spectral range of ∼ 1.2 − 16 μm. Measurements were carried out in a reflection geometry under normal incidence with linear polarization across the ribbons, using a gold mirror as a reference for normalization.

4.4 | SHG Measurements

SHG measurements were conducted using a modified focus-scan setup [27] (Figure S7), in which the SHG signal was recorded as the sample was translated along the optical axis through the excitation focus. Lateral positions were probed by moving the tilted sample within the focal plane. The excitation consisted of linearly p-polarized Gaussian pulses (orthogonal to the long axis of the nanoribbons and perpendicular to a side of the equilateral triangles) with pulse duration $\tau \approx 200$ fs and repetition rate $f =$ 76 MHz, generated by an optical parametric oscillator pumped by a Ti:Sapphire laser. The center wavelength λ_0 was tunable from 1.975 to 3.1 μm. Slight daily variations in pulse duration and repetition rate were observed and accounted for.

A half-wave plate and polarizer ensured linear polarization, while two 20 mm lenses focused the excitation beam (waists $\sigma = 11.8$, 13.8, and 17.0 μm characterized for $\lambda_0 = 1.975$, 2.3, and 3.1 μm, respectively, estimated from the intensity $I(x, y) \propto e^{-(x^2+y^2)/\sigma^2}$ as a function of lateral position (x, y) relative to the maximum). For the corresponding SHG signals, a reduction of the waist by $\sqrt{2}$ was assumed. Excitation from the back side avoided substrate absorption of the nonlinear signal emitted from the metallic structures placed on the front side. At the silicon interface, the incident angle was refracted from 45° in air to $\theta \approx 13°$ inside the substrate, as estimated from Snell's law with the refractive index of the material [45]. After collimation, the nonlinear signal was isolated with transmission filters, coupled into a multimode fiber, and detected by single-photon detectors based on InGaAs or Si ($\lambda_0 = 1.975$ μm). Signal spectra were verified using a Nireos interferometer-based spectrometer via Fourier-transformed autocorrelation. Power drifts during acquisition were below 1% over 20 − 30 min.

The average excitation power P_{ave} was measured before the focusing lens, and the SHG power P_{SHG} was extracted from the detector count rate, with both corrected for optical transmission. The SHG response was characterized as a function of excitation power for each region of interest. A quadratic dependence was observed and fitted, while detector dark counts and saturation were included in the model. The SHG conversion efficiency was defined as $\eta = I_{SHG,peak}/I^2_{0,peak}$. The excitation peak intensity inside the silver film followed as $I_{0,peak} = 2P_{peak}/A$, where P_{peak} is the peak power of a single pulse and A the illumination area. For oblique incidence, an area $A = \pi\sigma_0^2 \sec\theta$ was approximated for an ellipse defined from the beam waist σ_0 and incidence angle θ inside the silicon. The peak power was obtained from the average power as $P_{peak} = (f_{shape}/f\tau)P_{ave}$, where the factor $f_{shape} = 0.94$ corrects for lateral Gaussian pulse profiles.

4.5 | Theoretical Calculation of Enhancement Factors

We define the enhancement ratio as the SHG intensity produced upon transmission of light through nanostructured ultrathin metal films divided by that produced by extended homogeneous films. For simplicity, we restrict our calculations to ribbon arrays, although the approach can be readily extended to periodic arrays of triangles or other geometries by integrating over the two-dimensional in-plane coordinates.

We assume that the SHG intensity scales with the squared magnitude of the second-harmonic polarization, which, as a rough approximation, is taken to be locally proportional to the square of the linear electric field at the fundamental frequency ω. The electric near fields $\mathbf{E}_\omega^{NR}$ and $\mathbf{E}_\omega^{TF}$ right outside the surfaces of the metal nanoribbons (NRs) and uniform thin films (TFs), respectively, are obtained numerically, as detailed below. For homogeneous films, the numerical results are in close agreement with the analytical theory for planar interfaces [46].

15214095, 0, Downloaded from https://advanced.onlinelibrary.wiley.com/doi/10.1002/adma.75217 by Centrum Voor Wiskunde En Info (Cwi), Wiley Online Library on [11/11/2026]. See the Terms and Conditions (https://onlinelibrary.wiley.com/terms-and-conditions) on Wiley Online Library for rules of use; OA articles are governed by the applicable Creative Commons License

Because the crystal lattice of the metal is centrosymmetric, we only consider an SHG surface polarization in both the structured and uniform films. This quantity is proportional to the nonlinear surface susceptibility, which we assume to be local, independent of surface orientation, and unaffected by nanostructuring (i.e., identical in the two configurations). We further assume that the surface susceptibility is dominated by the surface-normal component $\chi^{\mathrm{SHG}}_{\perp\perp\perp}$. Consequently, the susceptibility enters the SHG far-field intensity as an overall multiplicative factor that cancels when taking the ratio of the nonlinear intensities generated by patterned and unpatterned films.

We thus have a surface polarization oriented perpendicular to the metal boundary, whose magnitude is proportional to the nonlinear susceptibility and to $|E_{\omega,\perp}|^2$. To determine the radiation reaching the detector, we invoke electromagnetic reciprocity rather than explicitly propagating the emitted second-harmonic field. Specifically, the coupling to the detected far-field mode is obtained from the normal electric-field component at 2ω generated when the structure is illuminated from the detection direction. The resulting SHG amplitude can therefore be expressed as an integral over the metal surface involving the product of the local fundamental-field factor $[E_{\omega,\perp}]^2$ and the corresponding reciprocal field at the second-harmonic frequency $E_{2\omega,\perp}$. For the illumination geometry considered here, translational symmetry along the invariant in-plane direction allows the surface integration to be reduced to a one-dimensional contour integral, as illustrated in Figure S10. From these considerations, the enhancement ratio reduces to

$$\text{SHG enhancement} = \left| \frac{\oint_{\mathrm{NR}} ds \left[E^{\mathrm{NR}}_{\omega,\perp}(\mathbf{r}_s)\right]^2 E^{\mathrm{NR}}_{2\omega,\perp}(\mathbf{r}_s)}{\int_{\mathrm{TF}} ds \left[E^{\mathrm{TF}}_{\omega,\perp}(\mathbf{r}_s)\right]^2 E^{\mathrm{TF}}_{2\omega,\perp}(\mathbf{r}_s)} \right|^2 \quad (1)$$

where the integrations are performed along the NR and TF boundaries, respectively. For the NR, the path forms a closed loop around a single ribbon, whereas in the TF it follows the upper and lower interfaces over a distance equal to the period of the corresponding patterned structure. We use s as the arc-length parameter along the respective contours. This model is used to generate the theoretical results shown in Figure 3.

4.6 | Simulation of Optical Electric Fields

Near fields in the nanostructures were calculated from 2D simulations in the frequency domain using COMSOL Multiphysics, introducing periodic boundary conditions along the lateral direction of array symmetry to emulate the periodic structure, and perfectly matched layers along the out-of-plane direction. We considered a p-polarized incident plane wave impinging on the air–Si interface at an angle of 45° and in-plane orientation as in the experiment. A Drude-like permittivity $\epsilon_m(\omega) = \epsilon_b - \omega_p^2/[\omega(\omega + i\xi\gamma)]$ was used for the metals, with parameters $\hbar\omega_p = 9.17$ eV, $\hbar\gamma = 21$ meV, and $\epsilon_b = 4$ for silver, and $\hbar\omega_p = 9.06$ eV, $\hbar\gamma = 71$ meV, and $\epsilon_b = 9.5$ in gold, as extracted by fitting measured optical data [47]. A correction factor ξ was introduced to account for additional damping produced by imperfections introduced during the fabrication process (see main text). More precisely, results are fitted with $\xi = 3$, 5, and 7 for films containing 14, 11, and 7 Ag MLs, respectively.

Acknowledgments

This work has been supported in part by the European Research Council (101141220-QUEFES), the European Commission (101135288-EPIQUE), the Spanish MICIU (PID2024-157421NB-I00 and Severo Ochoa CEX2024-001490-S), the CERCA program, the Basque Government (IT2133-26), and the Austrian Science Fund (10.55776/COE1, 10.55776/F71, and 10.55776/FG5).

Conflicts of Interest

The authors declare no conflicts of interest.

Data Availability Statement

The data that support the findings of this study are available from the corresponding author upon reasonable request.

References

1. B. Sain, C. Meier, and T. Zentgraf, "Nonlinear Optics in All-dielectric Nanoantennas and Metasurfaces: A Review," *Advanced Photonics* 1 (2019): 024002.

2. T. P. McKenna, H. S. Stokowski, V. Ansari, et al., "Ultra-Low-Power Second-Order Nonlinear Optics on a Chip," *Nature Communications* 13 (2022): 4532.

3. M. A. Adeshina and H. Kim, "Exploring the Frontier: Nonlinear Optics in Low Dimensional Materials," *Nanophotonics* 14 (2025): 1451–1473.

4. R. Luo, Y. He, H. Liang, M. Li, and Q. Lin, "Highly Tunable Efficient Second-harmonic Generation in a Lithium Niobate Nanophotonic Waveguide," *Optica* 5 (2018): 1006.

5. L. Qu, W. Wu, W. Cai, M. Ren, and J. Xu, "Second Harmonic Generation in Lithium Niobate on Insulator," *Laser & Photonics Reviews* 19 (2025): 2401928.

6. Y. Yamamoto, S. Yamaguchi, N. Yamada, K. Ueda, and T. Matsumoto, "Quasi-Phase-Matched Second-Harmonic Generation in a Periodic-Lens Sequence Waveguide with a Relatively Wide Wavelength-Tuned Width," *Japanese Journal of Applied Physics* 34 (1995): 6382.

7. R. W. Boyd, *Nonlinear Optics*, 3rd ed. (Academic Press, 2008).

8. M. Kauranen and A. V. Zayats, "Nonlinear Plasmonics," *Nature Photonics* 6 (2012): 737.

9. Z. Liang, J. Sun, Y. Jiang, L. Jiang, and X. Chen, "Plasmonic Enhanced Optoelectronic Devices," *Plasmonics* 9 (2014): 859.

10. X.-X. Wu, W.-Y. Jiang, X.-F. Wang, et al., "Inch-Scale Ball-in-Bowl Plasmonic Nanostructure Arrays for Polarization-Independent Second-Harmonic Generation," *ACS Nano* 15 (2021): 1291.

11. K. Lu, M. Luo, W. Gao, Q. J. Wang, H. Sun, and D. Nam, "Strong Second-Harmonic Generation by Sublattice Polarization in Non-Uniformly Strained Monolayer Graphene," *Nature Communications* 14 (2023): 2580.

12. S. Kim, J. E. Fröch, A. Gardner, C. Li, I. Aharonovich, and A. S. Solntsev, "Second-Harmonic Generation in Multilayer Hexagonal Boron Nitride Flakes," *Optics Letters* 44 (2019): 5792.

13. C. Trovatello, C. Ferrante, B. Yang, et al., "Quasi-Phase-Matched Up- and Down-Conversion in Periodically Poled Layered Semiconductors," *Nature Photonics* 19 (2025): 291.

14. M. Zielinski, D. Oron, D. Chauvat, and J. Zyss, "Second-Harmonic Generation from a Single Core/Shell Quantum Dot," *Small* 5 (2009): 2835.

15214095, 0, Downloaded from https://advanced.onlinelibrary.wiley.com/doi/10.1002/adma.75217 by Centrum Voor Wiskunde En Info (Cwi), Wiley Online Library on [11/11/2026]. See the Terms and Conditions (https://onlinelibrary.wiley.com/terms-and-conditions) on Wiley Online Library for rules of use; OA articles are governed by the applicable Creative Commons License

15. S. Ren, Z. Chen, S. Li, et al., "Resonance-Enhanced Second Harmonic Generation via Quantum Dots Integrated with Ag Nanoarrays," *Optical Materials Express* 11 (2021): 3223.

16. F. X. Wang, F. J. Rodríguez, W. M. Albers, R. Ahorinta, J. E. Sipe, and M. Kauranen, "Surface and Bulk Contributions to the Second-Order Nonlinear Optical Response of a Gold Film," *Physical Review B* 80 (2009): 233402.

17. R. W. Boyd, Z. Shi, and I. De Leon, "The Third-Order Nonlinear Optical Susceptibility of Gold," *Optics Communications* 326 (2014): 74.

18. H. Dai, L. Zhang, Z. Wang, et al., "Linear and Nonlinear Optical Properties of Silver-Coated Gold Nanorods," *The Journal of Physical Chemistry C* 121 (2017): 12358.

19. I. Abdelwahab, B. Tilmann, Y. Wu, et al., "Giant Second-Harmonic Generation in Ferroelectric $NbOI_2$," *Nature Photonics* 16 (2022): 644.

20. G. Zograf, A. Y. Polyakov, M. Bancerek, T. A. Antosiewicz, B. Küçüköz, and T. O. Shegai, "Combining Ultrahigh Index with Exceptional Nonlinearity in Resonant Transition Metal Dichalcogenide Nanodisks," *Nature Photonics* 18 (2024): 751.

21. N. Bernhardt, K. Koshelev, S. J. U. White, et al., "Quasi-BIC Resonant Enhancement of Second-Harmonic Generation in WS_2 Monolayers," *Nano Letters* 20 (2020): 5309.

22. T. G. Pedersen, K. Pedersen, and T. B. Kristensen, "Optical Second-Harmonic Generation from Ag Quantum Wells on Si(111) 7×7 : Experiment and Theory," *Physical Review B* 60 (1999): R13997.

23. H. Hirayama, T. Kawata, and K. Takayanagi, "Oscillation of the Optical Second-Harmonic Generation Intensity During Ag Thin Film Growth on a Si(111) 7×7 Surface," *Physical Review B* 64 (2001): 195415.

24. K. Pedersen, T. G. Pedersen, and P. Morgen, "Surface and Interface Resonances in Second Harmonic Generation from Metallic Quantum Wells on Si(111)," *Physical Review B* 73 (2006): 125440.

25. A. Rodríguez Echarri, J. D. Cox, F. Iyikanat, and F. J. García de Abajo, "Nonlinear Plasmonic Response in Atomically Thin Metal Films," *Nanophotonics* 10 (2021): 4149.

26. C. Pan, Y. Tong, H. Qian, et al., "Large Area Single Crystal Gold of Single Nanometer Thickness for Nanophotonics," *Nature Communications* 15 (2024): 2840.

27. P. K. Jenke, S. Abdullah, A. P. Weber, et al., "Few-Atom-Thick Silver Films for Enhanced Nanoscale Nonlinear Optics," *Nature Communications* 17 (2026): 8214.

28. Z. M. Abd El-Fattah, V. Mkhitaryan, J. Brede, et al., "Plasmonics in Atomically Thin Crystalline Silver Films," *ACS Nano* 13 (2019): 7771.

29. V. Mkhitaryan, A. P. Weber, S. Abdullah, et al., "Ultraconfined Plasmons in Atomically Thin Crystalline Silver Nanostructures," *Advanced Materials* 36 (2024): 2302520.

30. M. I. Stockman, "Nanoplasmonics: The Physics Behind the Applications," *Physics Today* 64 (2011): 39.

31. T. Cesca, G. Pellegrini, V. Bello, et al., "Nonlinear Optical Properties of Au–Ag Nanoplanets Made by Ion Beam Processing of Bimetallic Nanoclusters in Silica," *Nuclear Instruments and Methods in Physics Research B* 268 (2010): 3227.

32. N. Leopold, V. Chiş, N. E. Mircescu, et al., "One Step Synthesis of SERS Active Colloidal Gold Nanoparticles by Reduction with Polyethylene Glycol," *Colloids and Surfaces A* 436 (2013): 133.

33. S. R. Ahmed, J. Kim, V. T. Tran, T. Suzuki, S. Neethirajan, J. Lee, and E. Y. Park, "In Situ Self-Assembly of Gold Nanoparticles on Hydrophilic and Hydrophobic Substrates for Influenza Virus-Sensing Platform," *Scientific Reports* 7 (2017): 44495.

34. H.-C. Chiang, Y. Wang, Q. Zhang, and K. Levon, "Optimization of the Electrodeposition of Gold Nanoparticles for the Application of Highly Sensitive, Label-Free Biosensor," *Biosensors* 9 (2019): 50.

35. R. G. Parkhomenko, S. V. Trubin, A. E. Turgambaeva, and I. K. Igumenov, "Deposition of Pure Gold Thin Films From Organometallic Precursors," *Journal of Crystal Growth* 414 (2015): 143.

36. K. M. McPeak, S. V. Jayanti, S. J. P. Kress, et al., "Plasmonic Films Can Easily Be Better: Rules and Recipes," *ACS Photonics* 2 (2015): 326.

37. X. Sun, R. Hong, H. Hou, Z. Fan, and J. Shao, "Thickness Dependence of Structure and Optical Properties of Silver Films Deposited by Magnetron Sputtering," *Thin Solid Films* 515 (2007): 6962.

38. F. Kiani and G. Tagliabue, "High Aspect Ratio Au Microflakes via Gap-Assisted Synthesis," *Chemistry of Materials* 34 (2022): 1278.

39. N. J. Speer, S.-J. Tang, T. Miller, and T.-C. Chiang, "Coherent Electronic Fringe Structure in Incommensurate Silver–Silicon Quantum Wells," *Science* 314 (2006): 804.

40. J. Butet, P.-F. Brevet, and O. J. F. Martin, "Optical Second-Harmonic Generation in Plasmonic Nanostructures: From Fundamental Principles to Advanced Applications," *ACS Nano* 9 (2015): 10545.

41. A. Rossetti, H. Hu, T. Venanzi, et al., "Control and Enhancement of Optical Nonlinearities in Plasmonic Semiconductor Nanostructures," *Light: Science & Applications* 14 (2025): 192.

42. M. Mesch, B. Metzger, M. Hentschel, and H. Giessen, "Nonlinear Plasmonic Sensing," *Nano Letters* 16 (2016): 3155.

43. F. Schiller, J. Cordón, D. Vyalikh, A. Rubio, and J. E. Ortega, "Fermi Gap Stabilization of an Incommensurate Two-Dimensional Superstructure," *Physical Review Letters* 94 (2005): 016103.

44. H. Fukumoto, M. Miyazaki, Y. Aoki, K. Nakatsuji, and H. Hirayama, "Initial Stage of Ag Growth on Bi/Ag(111)$\sqrt{3} \times \sqrt{3}$ Surfaces," *Surface Science* 611 (2013): 49.

45. D. Franta, P. Franta, J. Vohánka, M. Čermák, and I. Ohlídal, "Determination of Thicknesses and Temperatures of Crystalline Silicon Wafers From Optical Measurements in the Far Infrared Region," *Journal of Applied Physics* 123 (2018): 185707.

46. L. Novotny and B. Hecht, *Principles of Nano-Optics* (Cambridge University Press, 2006).

47. P. B. Johnson and R. W. Christy, "Optical Constants of the Noble Metals," *Physical Review B* 6 (1972): 4370.

Supporting Information

Additional supporting information can be found online in the Supporting Information section.

Supporting File: adma75217-sup-0001-SuppMat.pdf.

15214095, 0, Downloaded from https://advanced.onlinelibrary.wiley.com/doi/10.1002/adma.75217 by Centrum Voor Wiskunde En Info (Cwi), Wiley Online Library on [11/11/2026]. See the Terms and Conditions (https://onlinelibrary.wiley.com/terms-and-conditions) on Wiley Online Library for rules of use; OA articles are governed by the applicable Creative Commons License